E. R. de los Rios, * *R. M. Andrews,* † *M. W. Brown,* *
*and K. J. Miller**

Out-of-Phase Cyclic Deformation and Fatigue Fracture Studies on 316 Stainless Steel

ABSTRACT Fatigue tests under torsion, push–pull, and in-phase and out-of-phase combinations of these two loading modes were performed at room temperature and 550°C on AISI 316 stainless steel specimens. During testing, the material cyclically hardened and created various stable dislocation substructures.

Uniaxial, torsional, and in-phase biaxial loading at 550°C produced directional cell structures with the dislocations tangled in diffuse cell walls. Out-of-phase biaxial loading, on the other hand, promoted the formation of more equiaxed cells where the dislocations were arranged in a dense, tangled network-type boundary with the misorientation across the boundary increasing with phase angle.

The fatigue fracture process was composed of two stages: initial crystallographic cracking for Stage I crack growth and a non-crystallographic, striated fracture surface during Stage II crack propagation. An estimation of the extent of Stage II growth was accomplished both empirically, by the analysis of striation spacing measurements, and theoretically, by deriving crack growth rate equations. By comparing these calculations with the actual test life, the relative importance of Stage I propagation was assessed.

For high strain fatigue lives of up to approximately 1500 cycles, the Stage I growth period was very short and could be neglected in total-life calculations; however, for lifetimes in excess of 10 000 cycles, the Stage I period should be considered.

Introduction

Multiaxial fatigue problems have been the concern of engineers for some considerable time, particularly since most engineering structures and components are subjected to complex loading patterns. It is not surprising, therefore, that these problems have attracted attention which is reflected by the growing number of relevant publications. Reviews by Brown and Miller (1), Krempl (2), and Toor (3) dealt in particular with in-phase proportional loading.

In many practical cases though, the multiaxial loads are out-of-phase producing a non-proportional pattern of the cyclic stress components. In spite of the importance of this case very limited results are available, for example references (4)–(8), and reviews are scarce (3)(9)(10). One important problem

* Department of Mechanical Engineering, University of Sheffield, Mappin Street, Sheffield S1 3JD, UK.
† Welding Institution, Abington Hall, Abington, Cambridge CB1 6AL, UK.

highlighted by these investigations is the choice of a criterion to correlate the endurance results. Some authors have proposed, for example total strain (7), plastic work per cycle (11), and the octahedral shear strain integrated through a loading cycle (8) as suitable parameters, each proposal having some degree of success.

In order to achieve a wide-ranging correlation one would suspect that the best parameters to use should relate to the nature of the fatigue process itself, namely the formation and propagation of a crack. In this respect Brown and Miller (1)(12) proposed that the two fundamental strains to consider in multiaxial fatigue studies are those which govern the direction of crack growth and the crack growth rate. Hence the maximum shear strain range and the normal strain on the plane of maximum shear respectively were jointly considered in correlating data. This approach was applied to tension–torsion, room temperature, out-of-phase tests on a 1 per cent Cr–Mo–V steel, and predictions were made not only of fatigue life, but also of the planes on which cracks formed (5).

In an extension of this work Jordan *et al.* (13) showed a strong strain path dependence of endurance. Pure torsion test results were compared with tests in which a short half cycle of axial strain was superimposed on the continous torsional cycle in such a way that the peak torsional strain still remained the point of cyclic reversal. Lifetime was reduced from 1400 to 380 cycles.

Strain path dependency is considered further in this investigation by studying (a) the cyclic deformation substructures of in-phase and out-of-phase test specimens, (b) the mechanism of Stage II crack growth, and (c) crack growth striation spacing.

Notation

a	Crack length
B	Crack growth law constant
b	Burger's vector
d	Dislocation cell size
h	Dislocation spacing
k	Cyclic strength coefficient
N	Number of cycles
n	Number of glide dislocations
r	Length of flow band
S	Flow stress in flow band
T	Tensile strength
β	Cyclic strain hardening exponent
γ	Shear strain
Δ	Range of strain
ε	Axial or normal strain
λ	Biaxiality factor $\Delta\gamma/\Delta\varepsilon$

μ	Shear modulus
ν	Poisson's ratio
ϱ	Dislocation density
σ	Normal stress
τ	Shear stress
ϕ	Phase lag of torsional strain

Subscripts

c	Cell diameter
f	Local to cell boundary
max	Maximum shear amplitude
p	Plastic
s	Back stress
t	Total strain
1, 3	Maximum and minimum principal values

Experimental details

The material used in this investigation was from a reference heat of AISI 316 stainless steel, known as RNL Material 83. The chemical composition in weight percentages was 0.06 C, 0.49 Si, 1.75 Mn, 17.68 Cr, 12.30 Ni, 2.34 Mo, 0.021 S, and 0.035 P. The material was tested as received, i.e., solution treated in vacuum at 1050°C for 30 minutes, followed by air cooling. The grain structure was equiaxed with a mean linear intercept of 19 μm (mean diameter 32 μm, ASTM grain size 8).

Fatigue tests were carried out at room temperature and at 550°C, on tubular specimens of 25 mm parallel gauge length with 22 and 16 mm outside and inside diameters respectively. Full details of the specimen configuration and of the multiaxial testing facility are given elsewhere (10)(14). The tests were conducted under strain controlled conditions with triangular waveforms for axial, and torsional applied strain, measured directly from the specimen gauge length. The axial load and torque were used to derive the stresses. For biaxial tests a biaxiality factor was defined by $\lambda = \Delta\gamma/\Delta\varepsilon$ with λ taking values of 1, 1.5, 2, and 4. For out-of-phase tests the phase angle ($\phi = 30, 45, 60, 75, 90$, and 135 degrees) was measured such that a positive phase shift implied that the axial waveform led the torsional waveform. The frequency of cycling was adjusted to give a maximum shear strain rate of 0.1 per cent per second. Failure was defined as a 2 per cent fall in load range below the stabilized cyclic hardening curve. Further details of the tests performed during the course of this investigation, together with an analysis of the data, are presented in (10) and (15).

The microscopic examination of the failed specimens was mainly by thin foil transmission electron microscopy (TEM) and by scanning electron microscopy (SEM). The foils for TEM were prepared in the usual way (16). Examination by TEM revealed the type of dislocation substructure developed under cyclic loading and of particular interest was the effect of non-proportional defor-

mation on substructural development. During the SEM examination, the type of fatigue fracture mechanism observed on the fracture surface was studied in detail. Similarly an assessment was made of the mode of growth of cracks by observation of the gauge surface of the specimen.

Stress–strain response

For the in-phase tests, stresses and strains were determined from the hysteresis loops closest to mid-life, following the methods described in (**17**) and (**18**). The stress analysis was developed (**10**) to find the maximum shear stress and strain in the out-of-phase tests. They were expressed according to the Tresca criterion in terms of the maximum shear stress amplitude $\tau_{max} = (\sigma_1 - \sigma_3)/2$ and the maximum shear strain amplitude $\gamma_{max} = (\varepsilon_1 - \varepsilon_3)$. Here σ_1, ε_1, and σ_3, ε_3 are,
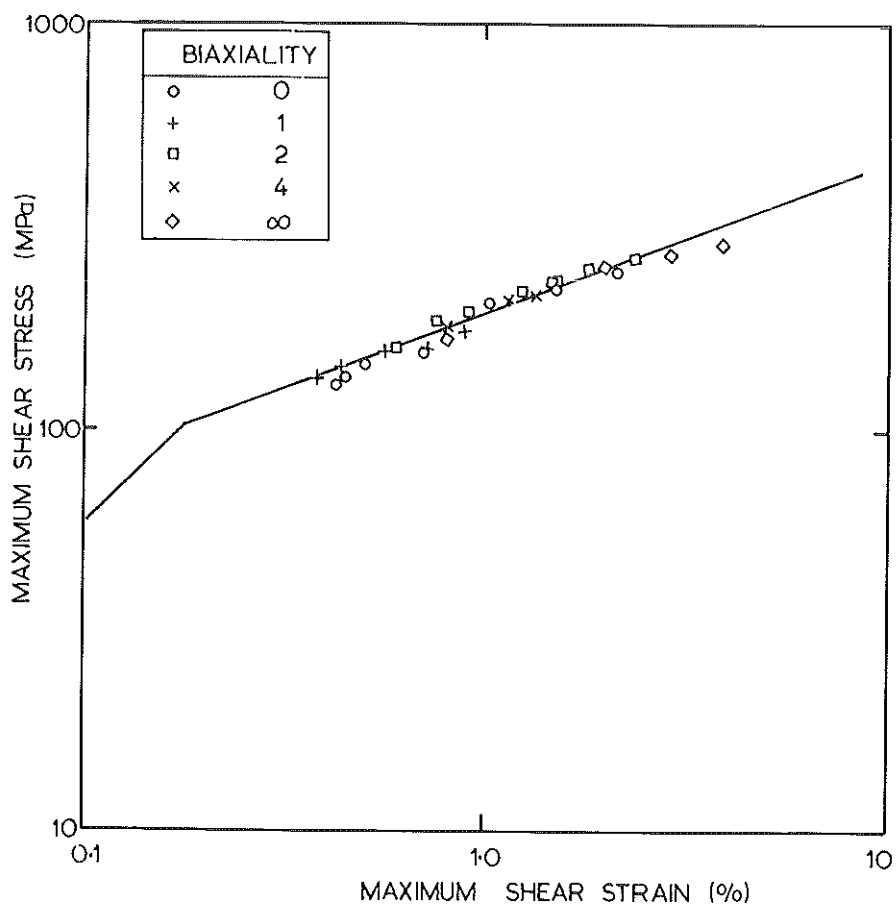

Fig 1   Stabilised cyclic stress–strain (τ_{max} vs γ_{max}) curves for in-phase loading at 550°C
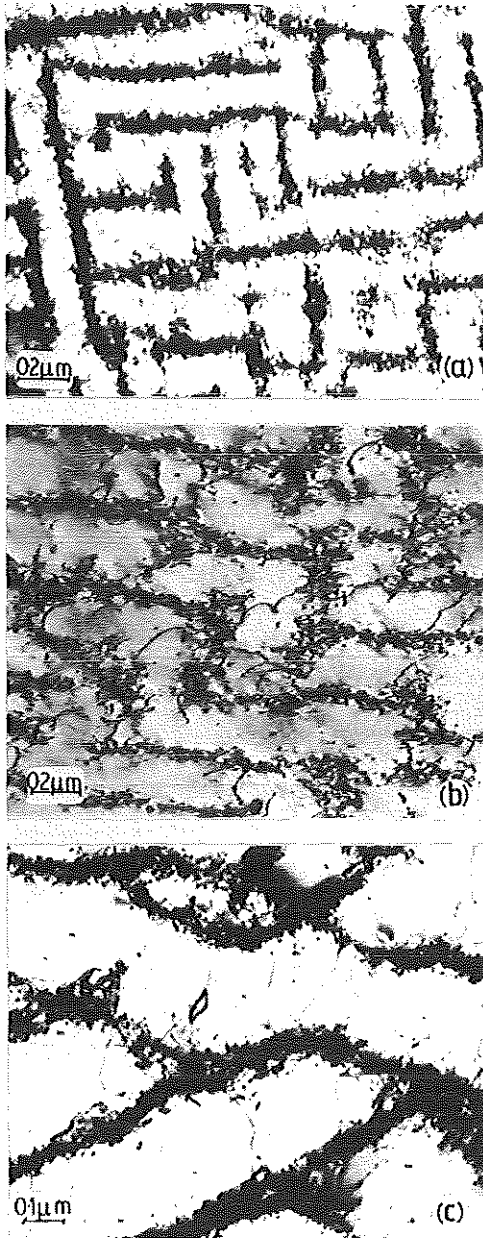
Fig 2   Dominant dislocation structures observed in specimens tested under: (a) torsional loading;
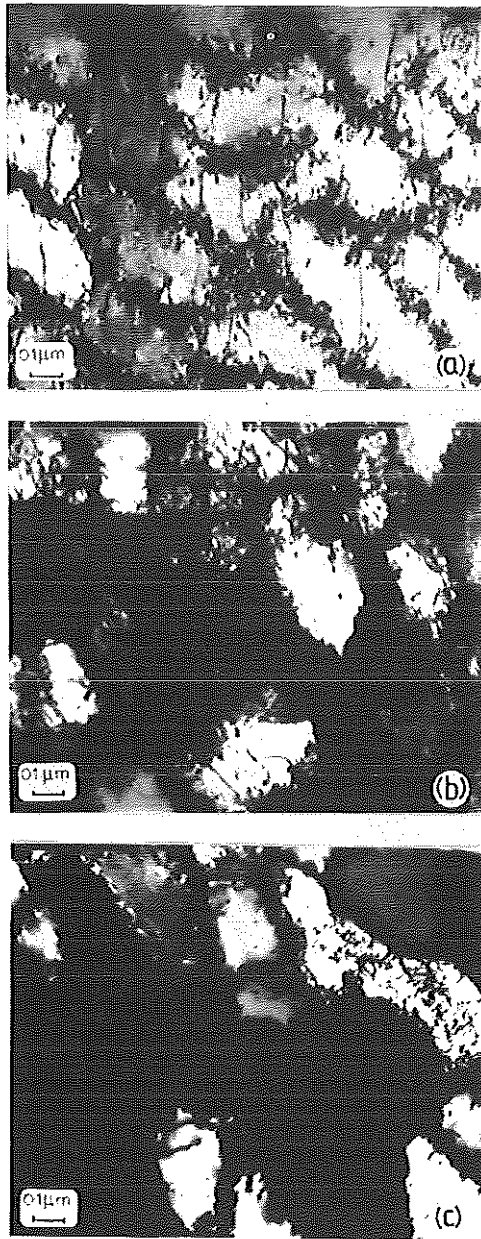(b) axial loading; (c) in-phase biaxial loading

Fig 3 Dominant dislocation structures observed in specimens tested under out-of-phase biaxial loading: (a) $\lambda = 1.5$ ($\Delta\gamma_t = 1.20$ per cent, $\Delta\epsilon_t = 0.82$ per cent), $\phi = 30$ degrees; (b) $\lambda = 1.5$ ($\Delta\gamma_t = 1.16$ per cent, $\Delta\epsilon_t = 0.79$ per cent), $\phi = 60$ degrees; (c) $\lambda = 1.5$ ($\Delta\gamma_t = 1.11$ per cent, $\Delta\epsilon_t = 0.74$ per cent), $\phi = 90$ degrees

Table 1 Dislocation densities and calculated flow stresses

Specimen No.	γ_{max} (%)	$\varrho\,(mm^{-2})$ $\times 10^{-8}$	$\varrho_t\,(mm^{-2})$ $\times 10^{-8}$	$\tau_f\,(N/mm^2)$ Equation (1)	$\tau_{max}\,(N/mm^2)$ Observed	$\tau_s\,(N/mm^2)$ Equation (2)	λ $(\Delta\gamma/\Delta\varepsilon)$	ϕ Degrees
87A	0.443	1.65	3.63	138	135		0	
34A	0.501	1.80	3.90	144	146		0	
93B	0.552	2.20	5.3	167	214	204	1.5	90
111B	0.575	9.95	5.1	164	194	180	1.0	90
120B	0.613	2.30	5.7	174	218	213	1.5	60
6A	0.701	1.95	4.8	160	158		0	
101B	0.705	2.0	5.5	170	194	186	1.5	30
96B	0.722	1.7	5.1	164	173		1.0	0
90B	1.138	2.0	7.7	202	212		4	0
12T	1.480	3.0	10	231	234			
20T	1.480	2.8	9.5	225	232			
33A	1.448	3.6	11	231	229		0	
1B	1.537	2.78	9.1	220	239		2.0	0
48B	2.406	2.85	10.2	233	268		2.0	0
11T	2.945	4.80	16.0	287	266			

respectively, the maximum and minimum principal values of stress and strain occurring at the time when γ_{max} attained its greatest value during the fatigue cycle (10).

The cyclic shear stress–shear strain curve for in-phase specimens tested at 550°C (see Fig. 1) shows that the Tresca criterion gives a good representation within the data scatter. Cyclic hardening showed the expected behaviour for low cycle fatigue; see (16) and (19). Rapid hardening was observed during the first 10 per cent or less of life, followed by constant or slightly falling loads. This behaviour suggests that the initial hardening reflects a dislocation multiplication and interaction, forming a stable structure which remains unaltered until failure. The dislocation structure at mid-life, when the stresses were calculated, is assumed therefore to be the same as that observed in the thin foils prepared after failure.

Figure 2 shows the dominant dislocation structures observed in the torsion, axial, and in-phase biaxial specimens, respectively. It shows that the dislocations are clustered together into diffuse cell walls, but in the case of torsion and axial specimens, the two-dimensional pattern is of a rectangular nature suggesting that in these two types of loading, the plastic deformation can be accomplished primarily by two main slip systems. The biaxial in-phase example (Fig. 2(c)) shows a less regular pattern of cell walls more typical of a material deformed by multiple slip.

Non-proportional test specimens showed, on the other hand, a fully developed cell structure with well defined cell boundaries (Fig. 3). An estimation of the dislocation density was made from the micrographs using a method described previously (16). Two measurements of the dislocation density were made; one related to the overall density (ϱ) the other to the localized cell boundary density (ϱ_f), see Table 1.

Flow stress calculations

The stress–strain relationship shown in Fig. 1 can also be obtained from the dislocation density values if suitable dislocation models are devised. The model chosen should represent closely the actual mechanism of plastic deformation, which is reflected by the dislocation structures observed. For a diffuse cell boundary structure a suitable dislocation model, used before with good results (16), gives the flow stress as that required to eject a dislocation loop from the cluster of dislocations at the cell boundary, thus

$$\tau_f = 0.5\mu b\varrho_f^{0.5} \tag{1}$$

where τ_f is the flow stress, μ is the shear modulus, b the Burgers vector, and ϱ_f the diffuse cell boundary dislocation density.

Calculated values of τ_f are given in Table 1 and are plotted in the shear stress–shear strain graph of Fig. 4 which illustrates that equation (1) correlates well with the experimental results for the torsion, uniaxial, and in-phase biaxial specimens. Figure 4 also shows that the experimental results of the out-of-phase
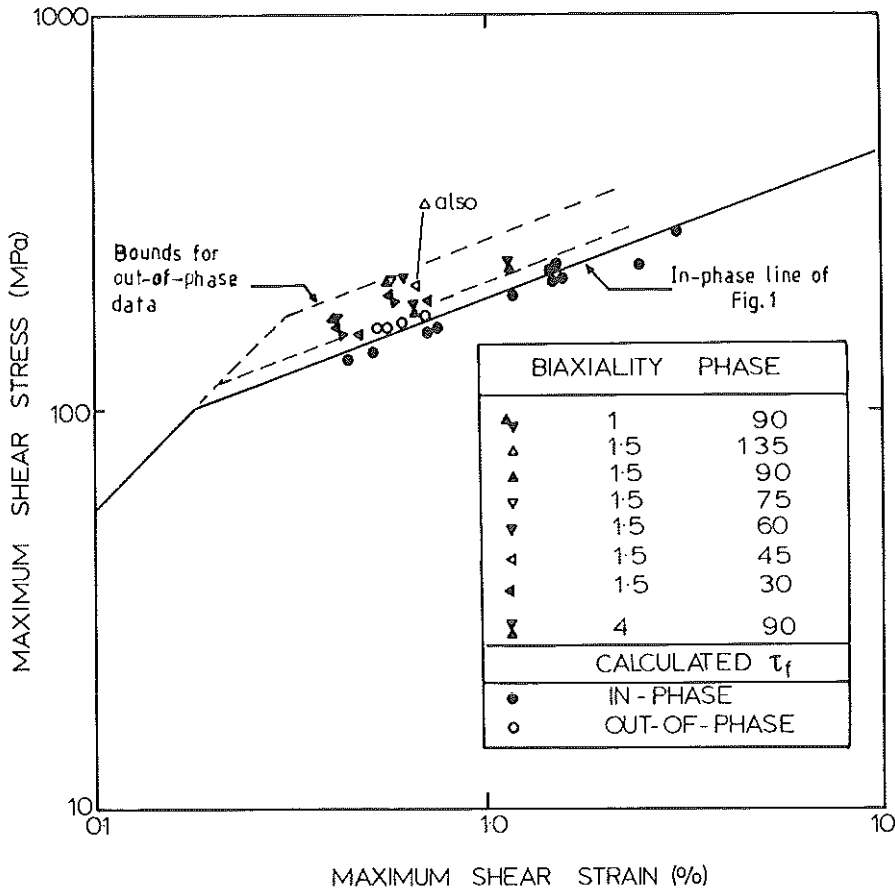
Fig 4   Experimental stress–strain (τ_{max} vs γ_{max}) results for out-of-phase test specimens and in-phase test baseline data, compared to calculated flow stresses (τ_f)

specimens invariably fall above the base line of the in-phase specimens. In other words, out-of-phase specimens hardened to a higher degree than for in-phase deformation. Figure 4 also shows that there is negligible difference between in-phase and out-of-phase calculations using equation (1) and that it is the out-of-phase calculations which give the largest discrepancy when compared to experimental results.

As mentioned previously, equation (1) describes strain hardening for a situation where the dislocations are closely tangled in diffuse cell walls. Microscopic evidence presented earlier showed that this was not the case for out-of-phase straining. Here the dislocations are condensed into properly defined cell boundaries, this is particularly so in a specimen with $\phi = 90$

degrees, $\lambda = 1.5$ where a definite misorientation is apparent between adjacent cells, Fig. 3.

For well defined cells, the arrangement of dislocations at the cell boundaries can be better modelled by finite walls of edge dislocations. These finite walls exert a back stress towards the interior of the cell which would have to be overcome for deformation to proceed by any freshly created slip bands. In other words, the maximum shear stress should equal the back stress, which is given by

$$\tau_s = \frac{\mu b}{2\pi} \varrho d_c \tag{2}$$

where ϱ is the overall dislocation density and d_c is the cell diameter. Values of τ_s for four specimens are given in Table 1 and plotted in Fig. 5, which shows that
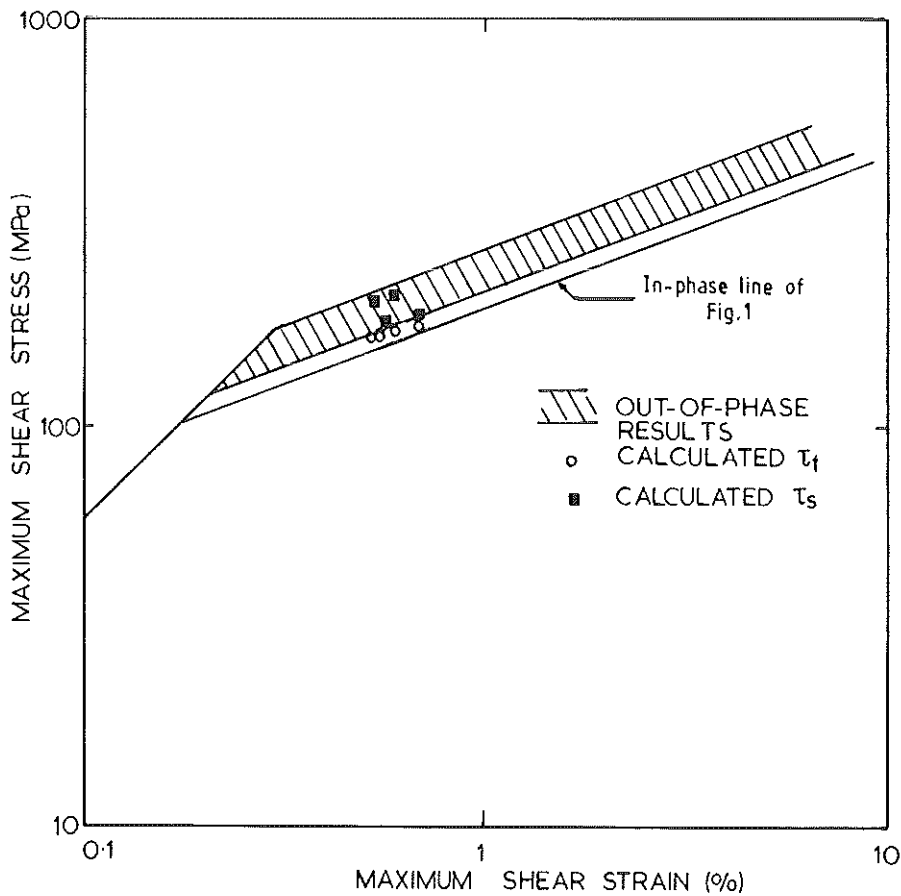

Fig 5   Comparison of flow stress values calculated from equation (1) for (τ_f) with those from equation (2) for (τ_s) under out-of-phase loading, and with the experimental data bands

equation (2) describes much more accurately the strain-hardening characteristics of specimens tested under non-proportional loading.

Fracture mechanics

In general, multiple surface cracks are formed during the initial part of the test; more cracks being observed at higher stress. The orientation of these surface cracks depends on the type of loading, for torsion loading cross-patterned cracks form at 45 degrees to the specimen axis, i.e., perpendicular to the maximum principal stress. These cross-pattern cracks are aligned in rows along the maximum shear directions (parallel and perpendicular to the specimen axis), so that they join up at an early stage to give propagating cracks along these shear planes. On the other hand, in push–pull and biaxial specimens, the macroscopic cracks (Stage II) propagate along a direction perpendicular to the maximum principal stress. Of all these crackss, only a few (1–5) propagate to failure. Figure 6 shows a section from a specimen incorporating the fracture surface and it shows that the failure crack is composed of four initially independent cracks.

   Observation of one crack in more detail (Fig. 7) shows that the fatigue crack can be divided into two main stages. Initially the crack growth is in Stage I along just one crystallographic plane of each grain, probably a slip plane, which is orientated at about 45 degrees to the specimen axis for this push–pull test. After propagating for approximately one or two grain diameters in this mode, the crack changes direction to continue its growth in Stage II along a direction perpendicular to the maximum normal stress. The fracture path, although still crystallographic, is not confined to one crystal plane, but crosses, in a stepped
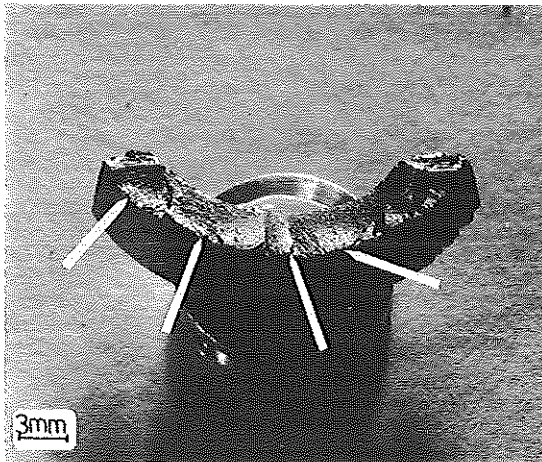

Fig 6   Fatigue fracture surface of a push–pull specimen ($\Delta \epsilon_t = 1.05$ per cent), showing four crack initiation sites
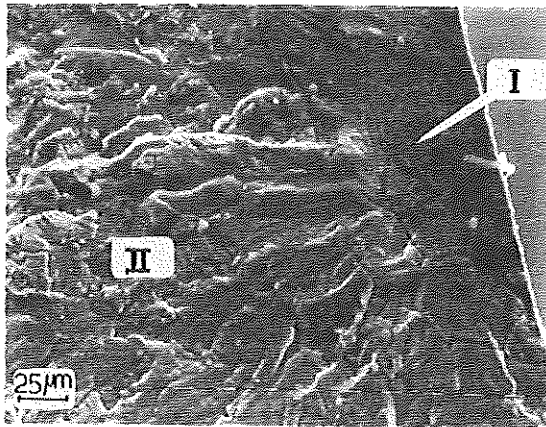
Fig 7   SEM fractograph showing Stage I crack propagation and the transition to Stage II, in push–pull loading
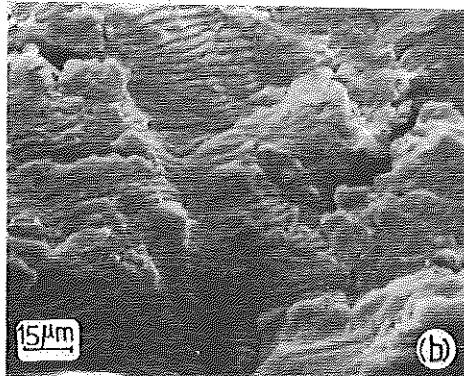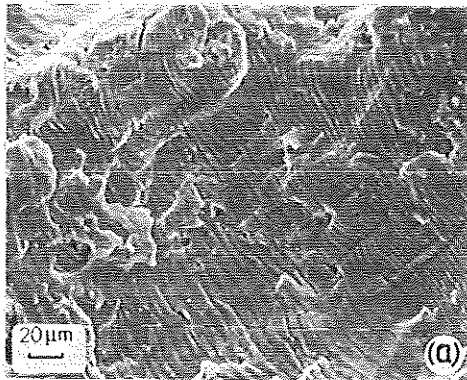

Fig 8   Stage II crack propagation of two specimens: (a) push–pull loading ($\Delta\epsilon_t = 1.20$ per cent); (b) out-of-phase biaxial $\lambda = 1.5$ ($\Delta\gamma_t = 0.80$ per cent, $\Delta\epsilon_t = 0.54$ per cent), $\phi = 90$ degrees
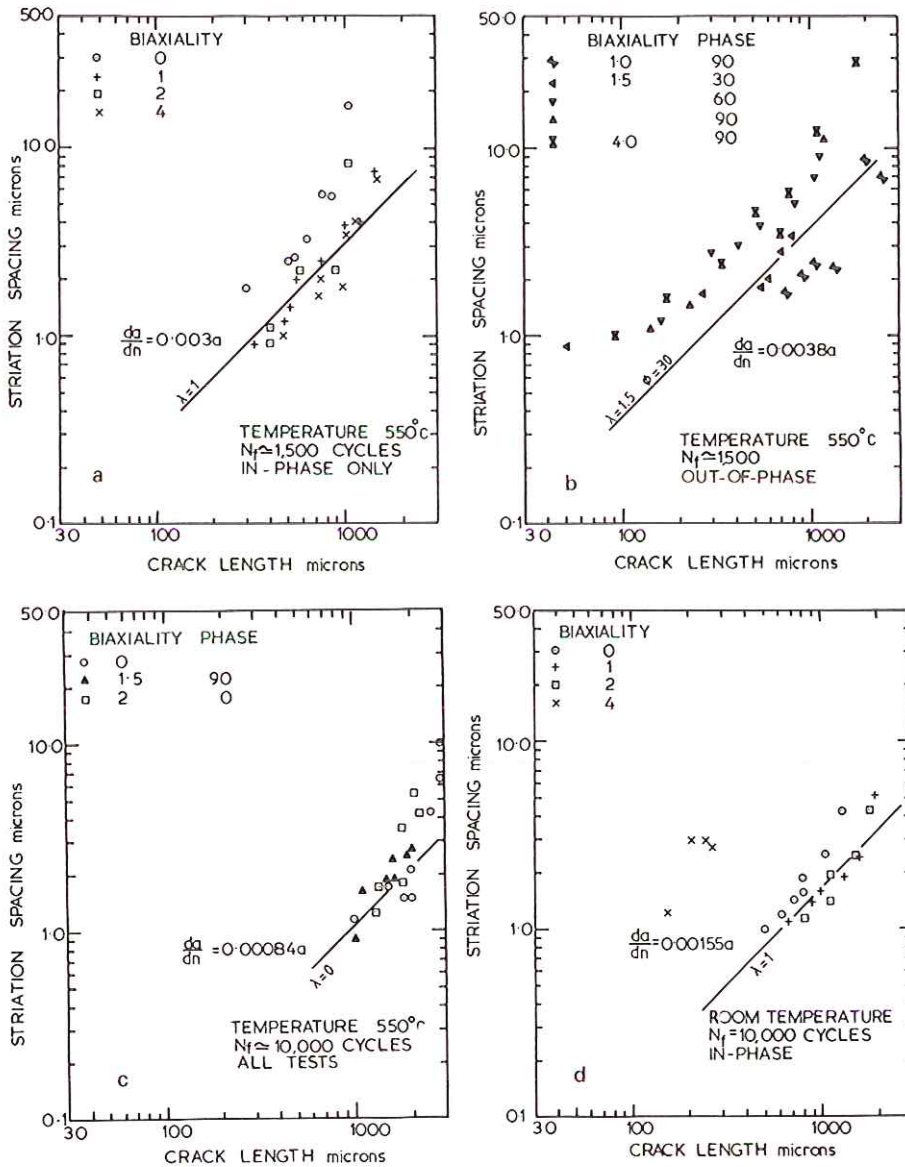
Fig 9 Striation spacings measurements plotted against distance from the crack initiation point (crack length) for: (a) temperature 550°C, endurance ~1500 cycles, in-phase; (b) temperature 550°C, endurance ~1500 cycles, out-of-phase; (c) temperature 550°C, endurance ~10 000 cycles, all tests; (d) room temperature, endurance ~10 000 cycles, in-phase
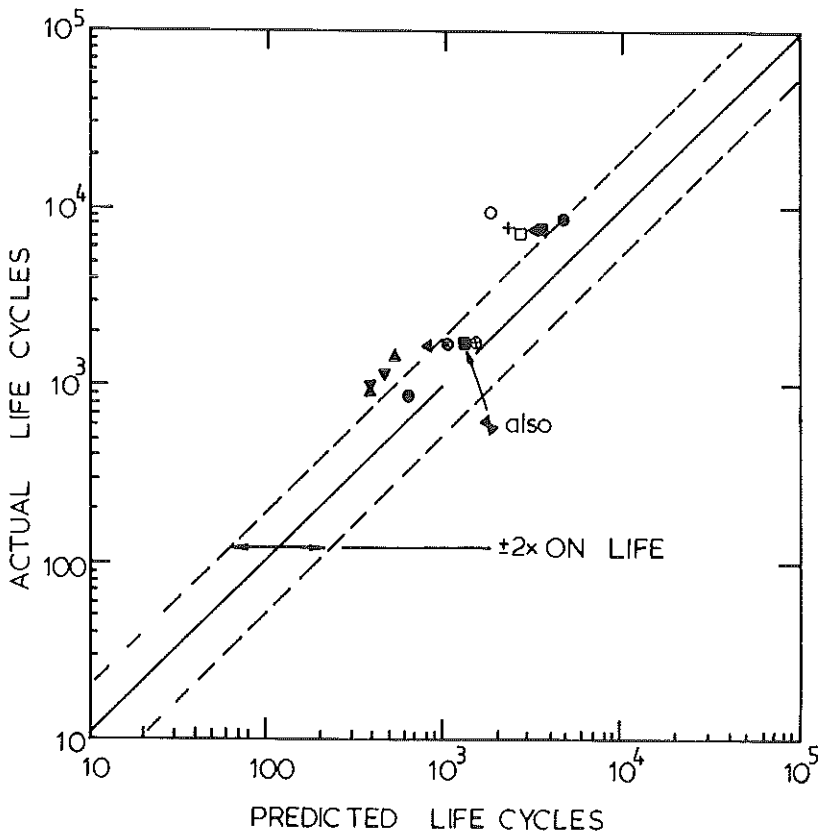
Fig 10   Prediction of crack propagation endurance based on integrated striation spacings

fashion, from one crystal plane to another to keep its broad front perpendicular to the maximum normal stress.

When the crack reaches 80–100 μm in length, the crystallographic mode ends and Stage II, striation fracture, begins. Figure 8 shows the striation fracture of (a) push–pull and (b) biaxial out-of-phase ($\lambda = 1.5$, $\phi = 90$ degrees) specimens, respectively. The similarities between the two fracture surfaces suggest that the fracture mechanism is the same, i.e., both cracks propagate under the opening mode, perpendicular to the maximum normal stress.

During the SEM examinations of the fractured surfaces, striation spacings were determined for selected specimens tested at 550°C and at room temperature, covering a wide range of biaxialities and phase angles. The results of these measurements are plotted in Fig. 9 as a function of crack length, that is the distance from the origin. Assuming that there is one-to-one correspondence between the striations and the number of cycles in these low cycle fatigue tests, then striation spacing represents the crack growth rate (da/dN). The functional trend of the relationship between crack growth rate and crack length for Stage II crack growth is given as a straight line in Fig. 9.

This functional relationship, expressed as $da/dN = Ba$, can be fitted to the experimental results for each of the specimens, and subsequently integrated from an initial crack length of 80 μm to a final crack length of 2000 μm. The lower limit corresponds to the distance from the crack initiation point to where the crack changes to striation crack propagation while the upper limit corresponds approximately to the point where the crack enters Stage III, the final fast stage of crack growth.

The predictions of striated crack propagation life obtained by the integration of these expressions are shown in Fig. 10 for two experimental test conditions giving fatigue lives in the range 1000–1500 cycles and 7000–10 000 cycles, respectively. Predictions for shorter lives (~1500 cycles) are better than those for longer lives (10 000 cycles); nevertheless the predictions are conservative in every case.

Crack growth models

Crack initiation is the result of localized plastic deformation in persistent slip bands around inclusions, etc., which leads to the formation of the fatigue crack. Crack growth is accomplished by discrete shear displacements of the material ahead of the crack. In Stage I crack growth the plastic deformation associated with the propagation of the crack is confined mainly to one plane, due of course to the reduced constraint imposed on the surface grains. This plane is usually a crystallographic plane. The crack advances along this plane to the first grain boundary, which represents a barrier to continued growth in the surrounding grains. Continued growth will be slower should the crack overcome the barrier, due to (a) the additional constraint provided by the grain boundary itself (which is considerable compared to the relative lack of constraint with a free surface

behind the crack tip), and (b) the change of crack path associated with the new crystallographic cracking plane. This will produce a complex three-dimensional fracture surface morphology (see Fig. 7) which further retards Stage I crack propagation. The change from the simple two-dimensional form of the Stage I fracture surface makes the striation mechanism of Stage II more favourable and the crack turns to become perpendicular to the maximum principal stress to facilitate continued growth.

The plastic deformation at the tip of the Stage II crack is accomplished by multiple slip which is assumed to be localized along flow bands at ±45 degrees to the plane of the crack. Striations, which are a fracture surface manifestation of crack extension, are the result of the relative displacements of the crack tip flanks along the flow bands as the crack opens and closes. Figure 11 shows this situation schematically. The faces of the crack slide apart, due to shear displacements along the flow bands of length r. The flow stress S along a band is

$$S = \frac{\mu n b}{r} \tag{3}$$

where

μ = shear modulus
n = number of glide dislocations in the band
b = Burgers vector

According to Tomkins (20) the extent of intense deformation at the crack tip in terms of the Bilby–Cottrell–Swinden model is

$$r = \frac{\pi^2}{2} \left(\frac{\tau_{max}}{2S} \right)^2 a \tag{4}$$

where τ_{max} is the applied maximum shear stress and a is the crack length.

Due to work hardening the local flow stress, S, must approach the tensile strength of the material, T, in the vicinity of the crack tip. Making this change,
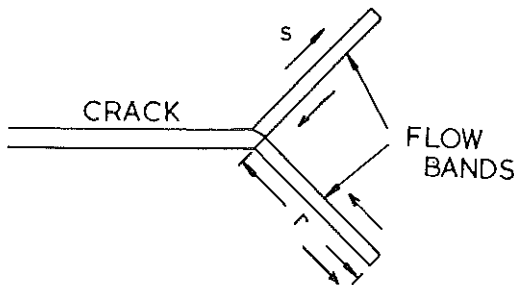

Fig 11   Schematic representation of the shear decohesion mechanism (38)

and assuming that crack growth rate is equal to the displacement along the flow band, nb, gives

$$nb = \frac{\mathrm{d}a}{\mathrm{d}N} = \frac{\pi^2}{8\mu} \frac{\tau_{max}^2}{T} a \tag{5}$$

Several other models of Stage II fatigue crack growth have been developed based on a shear decohesion mechanism (20)–(25); e.g., Tomkins derived the following expression for crack growth rate

$$\frac{\mathrm{d}a}{\mathrm{d}N} = \frac{\pi^2}{8} \frac{(k/T)^2 (\Delta\varepsilon_p)^{2\beta+1}}{2\beta + 1} a \tag{6}$$

where

β = cyclic stress–strain exponent
k = stress–strain coefficient for uniaxial stress–strain curve
$\Delta\varepsilon_p$ = plastic strain range

Crack growth expressions such as equations (5) and (6) may be integrated between the limits of 80 and 2000 μm to estimate the striation crack propagation life, which can be compared with Fig. 10. Results are presented in Fig. 12(a) for equation (5) and Fig. 12(b) for equation (6), taking $T = 465$ MPa (the tensile strength at 550°C (26)), $\beta = 0.288$, and $k = 1865$ MPa (10). In equation (6), the plastic strain range $\Delta\varepsilon_p$ was replaced by the equivalent expression $(2\gamma_{pmax})/(1 + \nu_p)$, where ν_p is 0.5, the plastic Poisson's ratio, so providing a multiaxial generalisation of the Tomkins' model.

Discussion

Non-proportional straining

For multiaxial deformation Brown and Miller (18) suggested that the Tresca criterion should be used to correlate cyclic stress–strain results in view of the fact that plastic deformation is accomplished by the movement of dislocations along slip planes aligned with the maximum shear plane. The results of previous investigations (27) and this study reiterate those findings for in-phase results.

Non-proportional loading, on the other hand, produced an extra hardening component above that determined by the Tresca relationship. Similar results were obtained by Kanazawa et al. (28) for a 1 per cent Cr–Mo–V steel, who credited this extra hardening to the rotation of the plane of maximum shear so that the preferential slip plane changes from one crystallographic system to another. The additional hardening was taken into consideration by introducing a rotation factor F related to the shear strains experienced by critical planes in the specimen.

For in-phase testing the relatively low plastic deformation imposed on the material during each cycle can be accommodated in most grains by the
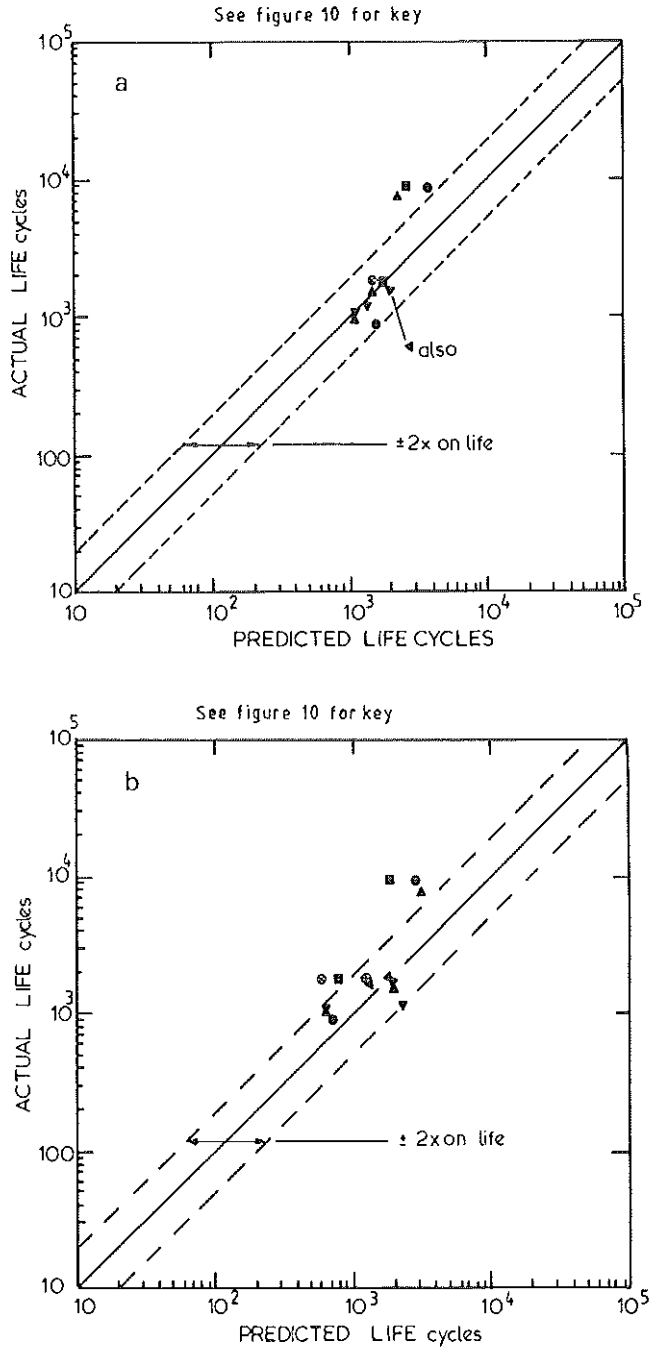
Fig 12 Prediction of endurance based on: (a) displacement along the flow band; (b) Tomkins'
model of crack growth (20)

operation of only a few slip systems, typically two for the special cases of torsion and push–pull, which result in regular dislocation patterns. Dislocations can, therefore, be either ejected from the diffuse walls or can transverse them cutting through the dislocation 'forest'. Both cases would produce a degree of hardening given by equation (1). In this context, and despite the high dislocation densities and tightly tangled appearance of many cell walls, there have been several reports that cell walls are penetrated by gliding dislocations (29)–(32).

The multiple slip brought about by constantly changing the preferential slip plane during a cycle in non-proportional loading makes the character of the cell boundary change from a loose tangle to a tight, dense network, increasing in perfection and misorientation as the phase angle is raised from 0 to 90 degrees.

The extra hardening developed by these latter dislocation arrangements when compared to the loose tangles, can be explained by the similar development which takes place in monotonic deformation (33). For low to medium plastic deformation cell structures are developed, characterized by relatively high boundary dislocation densities and fairly small angular misorientations between cells. When deformation is continued to large enough strains (higher flow stress) a marked increase in boundary perfection and misorientation is observed (34)(35). It seems, therefore, that both the character of the dislocation arrangements in the boundary as well as the substructural size must be considered to determine the strengthening behaviour of out-of-phase fatigue specimens.

Life predictions

One empirical and two theoretical methods were used to predict the life of the specimens. Each model predicts the short life test results (1500 cycles) better than the longer life (10 000 cycles), this is particularly true of the two theoretical methods. This is due to the relative importance, in terms of number of cycles, of the duration of Stage I and crystallographic crack growth. For high strain fatigue it has been suggested that the number of cycles for initiation is zero, cracks beginning to grow from the very first cycle (36)(37). The Stage I growth period is also thought to be short, so that most of the cyclic life corresponds to Stage II crack propagation. The close predictions afforded by the two theoretical methods in the high strain range also indicate that the crack growth equations represent fairly accurately Stage II crack growth. Crack growth, according to these models, is proportional to the plastic displacement along the flow bands emanating from the tip of the crack (shear band model) or to the crack tip opening displacement (Tomkins' model).

The empirical method of striation spacing is the least accurate, although always conservative, so predictions are on the safe side. One of the reasons for this lack of precision is that striations are only resolved in the SEM when their spacing is of the order of one micron, therefore no experimental data are available for the early period of Stage II growth when the spacing is much finer

than one micron. When making predictions in this phase, the crack is assumed to propagate at the rate determined by extrapolating the empirical crack growth equation back to 80 μm crack length.

Another reason for poor correlation is that striation spacing represents the local crack growth rate which can vary substantially along the crack front, and particularly from one grain to another, during the early stages of crack growth. This is manifested by the large scatter found for some of the striation spacing plotted in Fig. 9. It has also been reported that although sometimes the striation spacing represents one increment of crack advance in one cycle, this is not a general observation. For large crack openings multiple striations can be formed in one cycle, whilst for small crack openings it may take several cycles to create enough new surface at the tip for instability to occur (38).

The three methods give largely conservative predictions at 10 000 cycles, which is obviously caused by disregarding the crystallographic propagation phase in the life prediction analysis. The fracture surface, illustrated in Fig. 7, showed that in this material, Stage I is a crystallographic type of fracture. The crack propagates along just one slip band (plane) in the initial stages for a distance of one or two grain diameters. Cracks of this kind have been shown to be affected by microstructural features, in particular by grain or phase boundaries (39)–(41). Here a deceleration in crack growth usually takes place, the degree of which depends on crystal orientation and stress level. Therefore, the lower the stress level and longer the life, the higher is the proportion of total cyclic life in the Stage I period.

For the test conditions relevant to this investigation it seems that, for stress levels giving average lives of 10 000 cycles, the number of cycles for Stage I crack growth cannot be neglected. Obviously it is not possible to estimate Stage I lives from observation of fracture surfaces. Hence for these tests it would be necessary to obtain data of crack length versus number of cycles so that equations can be derived expressing crack growth rate as a function of material and mechanical parameters; similar to that reported in (37).

Conclusions

The Tresca criterion correlates well the cyclic stress–strain response of 316 stainless steel tested at 550°C under in-phase multiaxial conditions.

Extra cyclic hardening is observed in specimens tested under non-proportional loading, i.e., above that expected from the Tresca correlation. This is related to a change in the deformation substructure from one of preferentially oriented cells with diffuse cell boundaries to one of near equiaxed cells with tight, dense network-type boundaries; the latter increasing in perfection and misorientation with increasing phase angle.

Crack growth rate equations based on a Stage II crack growth type mechanism, together with empirical expressions obtained via striation spacing measurements, predict with reasonable accuracy lives of the order of 1500

cycles. The same methods show decreased accuracy in the region of 10 000 cycles to failure where Stage I crack propagation cannot be neglected.

Acknowledgements

Appendix

Derivation of the flow stress expression for a substructure with well developed cell boundaries

Well developed cell boundaries can be modelled by finite vertical walls of dislocations, of spacing h (Fig. 13(a)). The stress required to operate a dislocation source S is essentially the flow stress, which will have to overcome the back stress exerted by the dislocation wall towards the source.

Li (42) has calculated this stress as
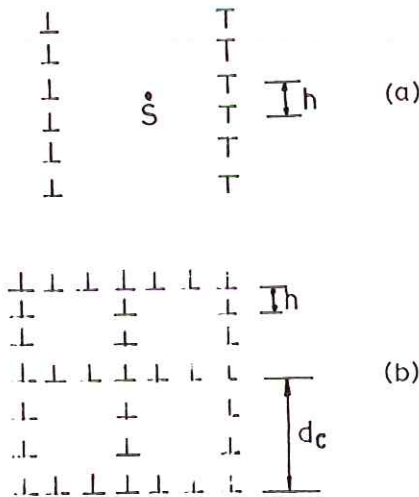
$$\tau_s = \frac{\mu b}{\pi h} \tag{7}$$

Fig 13   Schematic representation of the dislocation arrangements in a cell structure: (a) the wall arrangement of a cell boundary; (b) square grid arrangements of cells

For the sake of simplicity the cells are replaced by a square grid of dislocations (Fig. 13(b)). Therefore

$$h = \frac{2}{\varrho d_c}$$

thus the flow stress is

$$\tau_s = \frac{\mu b}{2\pi} \varrho d_c$$

ϱ = average dislocation density

d_c = cell size (0.4 μm)

μ = shear modulus = 5.83×10^4 N/mm^2

b = Burgers vector = 2.5×10^{-7} mm

The Burgers vector is the shortest lattice translation vector in the face-centred cubic structure of Fe_γ.

References

(1)   BROWN, M. W. and MILLER, K. J. (1982) Two decades of progress in the assessment of multiaxial low cycle fatigue life, *Low cycle fatigue and life prediction, ASTM STP 770*, ASTM, Philadelphia, PA, pp. 482–499.

(2)   KREMPL, E. (1974) The influence of state of stress on low-cycle fatigue of structural materials, *ASTM STP 549*, ASTM, Philadelphia, PA.

(3)   TOOR, P. M. (1974) A unified engineering approach to the prediction of multiaxial fatigue fracture of aircraft structures, *Engng Fracture Mech.*, 7, 731–741.

(4)   LITTLE, R. E. (1969) A note on the shear stress criterion for fatigue failure under combined stress, *Aeronaut. Q.*, 20, 57–60.

(5)   KANAZAWA, K., MILLER, K. J., and BROWN, M. W. (1977) Low-cycle fatigue under out-of-phase loading conditions, *J. Engng Mater. Technol.*, 99, 222–228.

(6)   DIETMANN, H. and ISSLER, L. (1974) Strength calculation under multiaxial out-of-phase fatigue loading, Conference on Dimensioning and Strength Calculations, Sixth Congress on Materials Testing, Budapest.

(7)   ZAMRIK, S. Y. and FRISHMUTH, R. E. (1973) The effects of out-of-phase biaxial strain cycling on low cycle fatigue, *Expl. Mech.*, 13, 204–208.

(8)   TAIRA, S., INOUE, T., and YOSHIDA, T. (1968) Low cycle fatigue under multiaxial stress (in the case of combined cyclic tension–compression and cyclic torsion out-of-phase at elevated temperature), 11th Japan Congress on Materials Research, Kyoto, pp. 60–65.

(9)   JORDAN, E. H. (1982) Fatigue multiaxial aspects in *A Decade of Progress*, American Society of Mechanical Engineers, New York, pp. 507–518.

(10) ANDREWS, R. M. (1968) *High temperature fatigue of AISI 316 stainless steel under complex biaxial loading*, PhD thesis, University of Sheffield, UK.

(11) GARUD, Y. S. (1981) A new approach to the evaluation of fatigue under multiaxial loading, *J. Engng Mater. Technol.*, 103, 118–125.

(12) BROWN, M. W. and MILLER, K. J. (1973) A theory for fatigue failure under multiaxial stress–strain conditions, *Proc. Instn mech. Engrs*, 187, 745–755.

(13) JORDAN, E. H., BROWN, M. W., and MILLER, K. J. (1985) Fatigue under severe non-proportional loading, *Multiaxial Fatigue, ASTM STP 853*, ASTM, Philadelphia, PA, pp. 569–585.

(14) BROWN, M. W. and MILLER, K. J. (1981) A biaxial fatigue machine for elevated temperature testing, *J. Testing Eval.*, 9, 202–208.

(15) ANDREWS, R. M. and BROWN, M. W. (1988) Elevated temperature out-of-phase fatigue behaviour of a stainless steel, *Biaxial and Multiaxial Fatigue*, EGF 3 (Edited by BROWN, M. W. and MILLER, K. J.), Mechanical Engineering Publications, London, pp. 641–658. This volume.

(16) de los RIOS, E. R. and BROWN, M. W. (1981) Cyclic strain hardening of 316 stainless steel at elevated temperatures, *Fatigue Engng Mater. Structures*, **4**, 377–388.

(17) BROWN, M. W. (1978) Torsional stresses in tubular specimens, *J. Strain Analysis*, **13**, 23–28.

(18) BROWN, M. W. and MILLER, K. J. (1979) Biaxial cyclic deformation behaviour of steels, *Fatigue Engng Mater. Structures*, **1**, 93–106.

(19) KANDIL, F. A., BROWN, M. W., and MILLER, K. J. (1982) Biaxial low cycle fatigue failure of 316 stainless steel at elevated temperatures, *Mechanical behaviour and nuclear applications of stainless steel at elevated temperatures*, Book 280, The Metals Society, London, pp. 203–209.

(20) TOMKINS, B. (1968) Fatigue crack propagation – an analysis, *Phil. Mag.*, **18**, 1041–1066.

(21) LAIRD, C. and SMITH, G. C. (1962) Crack propagation in high stress fatigue, *Phil. Mag.*, **7**, 847–857.

(22) HERTZEBERG, R. W. (1967) Fatigue fracture surface appearance, *ASTM STP 415*, ASTM, Philadelphia, PA, pp. 205–225.

(23) McMILLAN, J. C. and PELLOUX, R. M. N. (1967) Fatigue crack propagation under program and random loads, *ibid.*, pp. 505–553.

(24) TOMKINS, B. and BIGGS, W. D. (1969) Low endurance fatigue in metals and polymers, *J. Mat. Sci.*, **4**, 532–553.

(25) SPITZIG, W. H., TALOLA, P. W., and WEI, R. P. (1968) Fatigue crack propagation and fractographic analysis of 18 Ni (250) maraging steel tested in argon and hydrogen environments, *Engng Fracture Mech.*, **1**, 155–166.

(26) KANDIL, F. A., MILLER, K. J., and BROWN, M. W. (1985) Creep and ageing interactions in biaxial fatigue of Type 316 stainless steel, *Multiaxial Fatigue, ASTM STP 853*, ASTM, Philadelphia, PA, pp. 651–668.

(27) de los RIOS, E. R., KANDIL, F. A., MILLER, K. J., and BROWN, M. W. (1985) A metallographic study of multiaxial creep-fatigue behaviour in 316 stainless steel, *ibid.*, pp. 669–687.

(28) KANAZAWA, K., MILLER, K. J., and BROWN, M. W. (1979) Cyclic deformation of 1% Cr–Mo–V steel under out-of-phase loads, *Fatigue Engng Mater. Structures*, **2**, 219–228.

(29) THOMSON, A. W., BASKES, M. I., and FLANAGAN, W. F. (1973) The dependence of polycrystal work hardening on grain size, *Acta Met.*, **21**, 1017–1028.

(30) LANGFORD, G. and COHEN, M. (1975) Microstructural analysis by high-voltage electron diffraction of severely drawn iron wires, *Met. Trans*, **6A**, 901–910.

(31) RACK, H. J. and COHEN, M. (1970) Strain hardening of iron–titanium alloys at very large strains, *Mater. Sci. Engng*, **6**, 320–326.

(32) LI, J. C. M. (1963) Petch relation and grain boundary sources, *Trans TMS-AIME*, **227**, 239–247.

(33) THOMSON, A. W. (1977) Substructure strengthening mechanisms, *Met. Trans*, **8A**, 833–842.

(34) CAIRNS, J. H., CLOUGH, J., DEWEY, M. A. P., and NUTTING, J. (1971) The structure and mechanical properties of heavily deformed copper, *J. Inst. Metals*, **99**, 93–97.

(35) KALISH, D. and LeFEBVRE, B. G. (1975) Subgrain strengthening of aluminium conductor wires, *Met. Trans*, **6A**, 1319–1324.

(36) MILLER, K. J. (1985) Initiation and growth of short cracks, *Fundamentals of Deformation and Fracture*, Eshelby Memorial Symposium, Cambridge University Press, pp. 477–500.

(37) HOBSON, P. D., BROWN, M. W., and de los RIOS, E. R. (1985) Two phases of short crack growth in a medium carbon steel, *The Behaviour of Short Fatigue Cracks*, EGF 1 (Edited by MILLER, K. J. and de los RIOS, E. R.), Mechanical Engineering Publications, London, pp. 441–460.

(38) TOMKINS, B. (1981) Fatigue: Mechanisms, in *Creep and Fatigue in High Temperature Alloys*, Applied Science, New York, pp. 111–143.

(39) LANKFORD, J. (1982) The growth of small fatigue cracks in 7075-T6 aluminium, *Fatigue Engng Mater. Structures*, **5**, 233–248.

(40) de los RIOS, E. R., TANG, Z., and MILLER, K. J. (1984) Short crack fatigue behaviour in a medium carbon steel, *Fatigue Engng Mater. Structures*, **7**, 97–108.
(41) de los RIOS, E. R., MOHAMED, H. J., and MILLER, K. J. (1985) A micro-mechanics analysis for short fatigue crack growth, *Fatigue Engng Mater. Structures*, **8**, 49–63.
(42) LI, J. C. M. (1963) Theory of strengthening by dislocation groupings in *Electron Microscopy and the Strength of Crystals* (Edited by THOMAS, G. and WASHBURN, J.), Interscience, New York, pp. 713–779.